Single-shot dual-mode water-immersion microscopy platform for biological applications

JOSÉ ÁNGEL PICAZO-BUENO,[1] DAN COJOC,[2] FEDERICO ISEPPON,[3] VINCENT TORRE,[3] VICENTE MICÓ[1,*]

[1]Universidad de Valencia, Departamento de Óptica y Optometría y Ciencias de la Visión, C/Doctor Moliner 50, Burjassot, Spain, 46100.
[2]CNR-IOM Institute of Materials, Area Science Park - Basovizza, S.S. 14 km 163.5, Trieste, Italy, 34149.
[3]SISSA – International School for Advanced Studies, Via Bonomea, 265, 34136 Trieste, Italy.
*Corresponding author: vicente.mico@uv.es

A single-shot water-immersion digital holographic microscope combined with broadband (white light) illumination mode is presented. This double imaging platform allows conventional incoherent visualization with phase holographic imaging of inspected samples. The holographic architecture is implemented at the image space (that is, after passing the microscope lens) thus reducing the sensitivity of the system to vibrations and/or thermal changes in comparison to regular interferometers. Because of the off-axis holographic recording principle, quantitative phase images of live biosamples can be recorded in a single camera snapshot at full-field geometry without any moving parts. And the use of water immersion imaging lenses maximizes the achievable resolution limit. This dual mode microscope platform is first calibrated using microbeads, then applied to the characterization of fixed cells (neuroblastoma, breast cancer and hippocampal neuronal cells) and finally validated for visualization of dynamic living cells (hippocampal neurons). © 2017 Optical Society of America

1. INTRODUCTION

Dynamic process visualization at cellular level without influencing the process itself is a particularly useful tool in biomedical imaging. In that sense, photo-damage of the cells should be avoided since physiological changes induced by excessive illumination can lead to artefacts and abnormal responses [1, 2]. Therefore, linear optical techniques requiring low light intensities are preferable. But even in this case, illumination with an innocuous wavelength is still important since, otherwise, it can influence or disturb the behaviour of the sample thus yielding in wrong cell's dynamics and inappropriate conclusions. Just as a couple of examples, pulsed laser light is able to modulate the growth of axons of primary neuronal cell cultures [3] and aggregation of red blood cells has been shown to be wavelength dependent [4].

Inside linear imaging modality methods, digital holographic microscopy (DHM) has becoming a powerful and versatile tool in many significant fields of Biophotonics, Life Sciences and Medicine [5-7]. DHM combines into a single platform high-quality imaging provided by microscopy, whole-object wavefront recovery provided by holography, and numerical processing capabilities provided by computers [8-12]. DHM allows visualization of phase samples using a non-invasive (no need for stained samples), full-field (non-scanning), real-time (on-line control), non-contact (no sample damage) and static (no moving components) operating principle [13, 14].

DHM originates from the application of digital holography (DH) to microscopy in order to magnify the object's diffracted wavefront previously to be electronically sampled in the recording process. DH seems to start approximately half a century ago [15, 16] and it is based on the same holographic principles than classical holography but replacing the holographic recording medium by electronic image recording devices (typically a CCD or a CMOS camera). Thus, a complete parallelism can be established between classical and digital holography and the extension to DHM is straightforward.

Since the first evidences on DHM [17-19], a wide range of applications have been reported in the literature enabling DHM as a high-resolution multi-in-focus imaging method for polarization microscopy imaging [20], aberration lens compensation [21], particle tracking [22], extended depth of field imaging [23], micro-electromechanical systems inspection [24], 3-D dynamic analysis of cells [25] and refractive index characterization [26-28], just to cite a few. Because of its interferometric underlying principle, DHM has been implemented using different classical interferometric configurations [29-34] being the most used one the Mach-Zehnder interferometric layout [8, 9, 11, 12, 17, 19]. Nevertheless and considering illumination by transmission, common-path interferometric (CPI) configuration [35-51] provides significant advantages over all previous architectures. In CPI, both the imaging and the reference beams follow nearly the same optical path because both are transmitted in parallel through the same

microscope lens. Thus the instabilities of the system (mechanical vibrations or thermal changes between both optical paths) do not affect the obtained results.

Roughly speaking, CPI can be divided into three general types of layouts. As first, the imaging beam allows the synthesis of the reference beam after passing the microscope lens [35-39]. Once the transmitted beam is split into two beams, one of them is spatially filtered by using a pinhole mask at an intermediate Fourier plane. The filtering process allows reference beam synthesis by DC term transmission and sample's information blocking. Its main advantage is that the field of view (FOV) is fully preserved while the strong drawback is the need to implement a relatively complex opto-mechanical stage at the microscope's exit port. As an additional implementation, the use of spatial light modulators for in-line generation of the reference beam has also been reported in the literature [40-42].

Second and supposing that the sample is sparse, the surroundings of the inspected sample area can act in good approximation as a clear region for reference beam transmission. Once transmitted through the objective lens, it is only a question of overlap the imaging beam with a shifted version of itself since it is assumed that there is a blank or clear region without sample information in the imaging beam which is considered to not alter the light passing through it [43-47]. This type of CPI can be easily assembled (less optical elements, more compact and simple configuration, etc.) than the previous one but its applicability is restricted to sparse samples. Nevertheless, this is a common fact in many cases when imaging biosamples.

And third, the reference beam can be transmitted in parallel with the imaging beam through the microscope lens without any approximation. Once transmitted, both beams are properly overlapped at the recording plane [48-51]. This type of parallel transmission can be accomplished by the specific constraints of the input plane design: a black region at the input plane in side-by-side configuration with the sample [48-50] or by back-reflection at the tilted coverslip of a specially designed chamber [51] for transmissive and reflective configurations, respectively. And after that, both beams are overlapped allowing holographic recording by using minimal elements (diffraction gratings and tube lenses). This type of CPI allows reference beam transmission for all sample cases by minimal modifications in the setup with the inconvenience of a specific input plane spatial distribution design.

In this paper, we report onto a home-built platform based on single-shot immersion DHM technique in combination with broadband (white light) illumination and visualization. This double mode imaging platform combines real-time conventional incoherent visualization with off-line quantitative phase holographic imaging at diffraction-limited resolution level due to the use of water-immersion microscope lenses. In order to improve robustness of the system considering vibrations and/or thermal changes, the interferometric stage is assembled by synthesizing the reference beam after passing the objective lens. Due to the off-axis holographic recording principle, quantitative phase images of live biosamples are recorded in a single camera snapshot at full-field geometry without any moving parts. The capabilities of this dual mode microscope platform are experimentally validated by first using microbeads for calibration, then imaging fixed cells (NG108 neuroblastoma, breast cancer cells (MDA-MB-231) and hippocampal neuronal cells) under different visualization modes, and finally for visualization of dynamic samples (growth cones of hippocampal neurons).

2. DESCRIPTION OF THE IMAGING PLATFORM

The experimental layout is presented in Fig. 1. It is a dual imaging platform containing incoherent (white light) and coherent (infrared laser source) illuminations combined by a dichroic mirror (DM1). The broadband illumination is used for general imaging purposes (centering

the sample, imaging with reduced noise, etc.) and it is reflected out from the coherent path by a second dichroic mirror (DM2) after passing the tube lens which is also used to image the sample onto the CCD plane (CCD1). The coherent illumination is aligned with the incoherent one following the same optical path until DM2 where becomes transmitted allowing the assembly of a home-built Mach-Zehnder interferometric architecture. This optical layout is set in vertical (see Fig. 1) but the interferometric stage is built in the horizontal plane for simplicity. Nevertheless and for the sake of simplicity, Figure 1 presents such assembly also in the vertical plane.
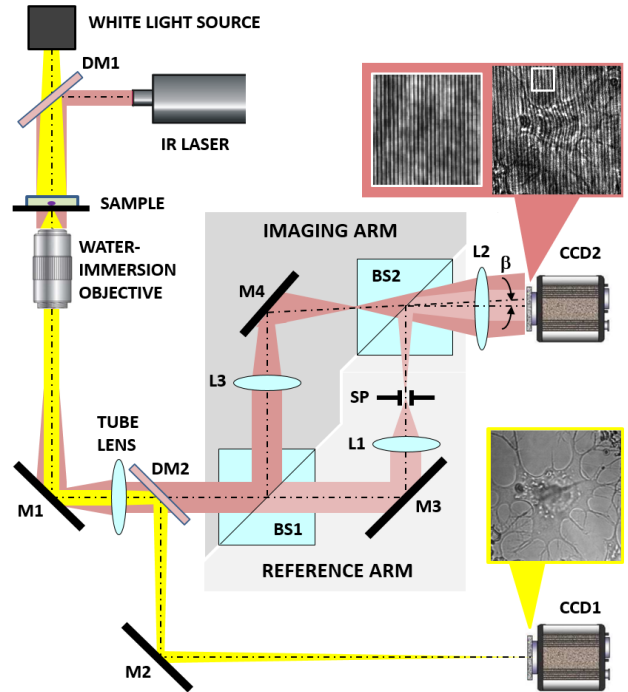

Fig. 1. Experimental layout for the proposed dual mode microscope platform. DM1, DM2, dichroic mirrors; M1, M2, M3, M4, metallic mirrors; BS1, BS2, beam splitters; L1, L2, L3, lenses; CCD1, CCD2, digital cameras; SP, spatial filter.

As we have previously stated, the interferometric configuration belongs to a CPI architecture where the reference beam is synthesized from the imaging beam at the image space after passing the microscope lens. A first non-polarizing beam splitter (BS1) divides the imaging beam into two coherent beams, one following the imaging arm while the other is used for reference beam generation. In the reference arm, a first lens (L1) focus the imaging beam and a spatial filter (SP) is properly selected and placed in order to transmit only the DC term of the focused imaging beam. It is a conventional spatial filtering using a pinhole and permits the generation of a clear reference beam from the imaging beam. Thus assembled, the pinhole position depends on the spatial location of the transmitted DC term which in turn directly depends on the sample's illumination direction. This fact makes the spatial pinhole position sensitive to misalignments in the laser beam propagation direction but remains unaffected once the laser source is fixed.

The reference beam is then reflected at a second non-polarizing beam splitter (BS2) which acts as combiner with the imaging beam coming from the imaging arm. This imaging beam is reflected at the first beam splitter (BS1) and passes through a third lens (L3) which is identical to the lens L1 to simplify the setup. After passing through the second beam splitter (BS2), an additional lens (L2) is used to make equal the divergence of both beams as they were before being split at BS1. Finally, a second CCD camera (CCD2) records the holograms

incoming from the combination of the two coherent beams. But to allow off-axis interferometric recording, the mirror M4 of the imaging arm is tilted to allow a relative bias (β) between both interferometric beams when reaching the CCD2. The recorded holograms are image plane holograms since the CCD2 is placed at the focal plane of the tube lens, something that also happens with the CCD1 by setting equal in the layout the distance between both CCD cameras and the tube lens. Thus, the only restriction is to assemble the interferometric stage in the optical path length provided by the focal length of the lenses L1-L3 Additional metallic mirrors (M1, M2, M3 and M4) fold the light path into proper directions and complete the experimental layout. Just as an example, Fig. 1 includes the images provided by both CCD cameras when using a NG108 neuroblastoma cell. The holographic image includes a magnified area to clearly show the interference fringes. The global structure of the cell is qualitatively visualized in the incoherent image while quantitative measurements will be derived from the coherent image as we will see in the experimental section.

Concerning the numerical processing for retrieving the complex amplitude distribution of the sample in the DHM imaging path, we have implemented a method based on spatial filtering at the Fourier plane from the recorded off-axis holograms [52-54]. Thus, the complex amplitude distribution of the transmitted frequency band-pass is recovered by applying a Fourier transformation over the recorded holograms and considering a circular spatial filtering mask at the distribution located at one of the diffraction orders. After filtering and centering process at the Fourier domain, each recovered elementary pupil can be digitally manipulated for aberration compensation [21] and numerically processed in order to propagate them to different planes [10, 53, 54]. This issue is of particular significance provided that the sample will exhibit some axial movement thus incurring in a retrieved blurred image which must be properly managed (as we will show in the experimental section).

3. EXPERIMENTAL RESULTS

The optical layout presented in Fig. 1 is assembled at the lab. It includes a white light source (high-power plasma light source - HPLS343, Thorlabs, USA) as incoherent illumination and an infrared CWA Laser (780 nm, 120 mW maximum optical power, 10 mW estimated used optical power, 10 cm coherence length, Omicron-Laser) as coherent illumination. Note that the use of a near infrared laser at 780 nm drastically reduces light absorption by the sample and hence living cell experiments are possible without damaging or influencing cell physiology. The samples are magnified and imaged by the combination of a water immersion microscope objective (100X, 1.0 NA, Olympus, Japan, 1 mm WD, 1.8 mm focal length) with a tube lens (200 mm focal length). The interferometric stage uses lenses (L1, L2, L3) with identical focal length f' = 100 mm, 25 mm side beam splitters (BS1, BS2) and a pinhole of diameter equal to 10 μm as spatial filter. Finally, two CCD cameras (Thorlabs DCC1240C, 5.3 μm pixel size, 25.8 fps, 1280x1024 pixels and Fastec Imaging HiSpec 4, 8 μm pixel size, 1696x1710 pixels) are used as digital recording devices for incoherent and coherent illuminations, respectively. Under these conditions, the depth of field (DOF) provided by the microscope objective is around 1 μm according to the formula $DOF = \lambda n_{medium}/NA^2$ and the global magnification of the system built at the lab is M ≅ 110 calculated as the ratio between the focal length of the tube lens and the one from the objective.

Now, experimental validation of the proposed dual-mode imaging platform is considered. As first, we present the calibration of the DHM modality using different types of microbeads (45 and 3 μm in diameter and a conical microbead). Then, experiments involving different types (NG108 neuroblastoma, breast cancer and hippocampal neuron cells) of static biosamples are imaged by the proposed platform.

A. Calibration of the DHM platform

Microbeads are the perfect sample for calibration purposes since they are microspheres of a single material (silica, polystyrene, etc.) from which refractive index at the illumination wavelength is perfectly known. The beads are deposited in aqueous suspension and are observed under DHM imaging modality. Figure 2 illustrates the full process when a 45 μm silica bead is imaged: (a) the recorded hologram, (b) its digital Fourier transformation (FT), (c) the retrieved (wrapped) phase distribution after filtering one of the diffraction orders at (b) and performing inverse FT, (d) the unwrapped phase distribution where the scale indicates radians of phase delay, and (e)-(f) are thickness distribution plots derived from the phase values.
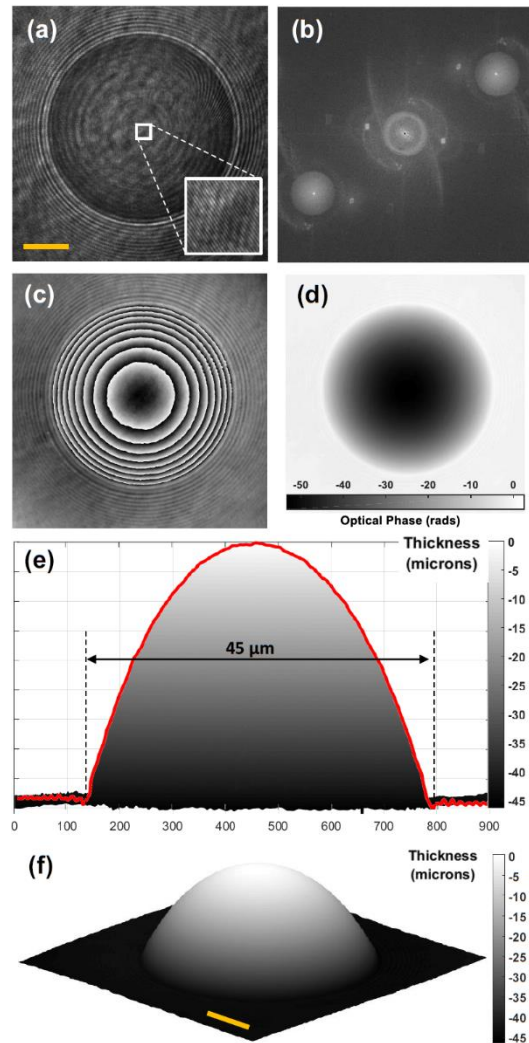

Fig. 2. Experimental results involving a 45 μm microbead imaged by DHM: (a) the recorded hologram (the inset is a magnified area to clearly show the interferometric fringes); (b) the FT of (a) showing the hologram diffraction orders; (c) the retrieved wrapped phase distribution coming from (b) after Fourier domain filtering and centering process; (d) the unwrapped phase distribution derived from (c); (e) the thickness profile from (d) and computed according to Eq. 1; and (f) 3D plot of the thickness info. Orange scale bars are 10 μm.

Thickness information is not directly related with the 3D geometry of the inspected sample but with the phase delay introduced by it, phase delay regarding the light passing through clear areas without sample. In such a way, a microbead will not appear as a ball-sphere under

thickness visualization mode but the maximum height of the thickness profile will be related with the maximum phase delay introduced by the microbead or, in other words, with its diameter. So, thickness distribution retrieved from microbeads is useful to characterize the performance of DHM. Thus, once the phase distribution $\Delta\varphi(x,y)$ is retrieved and unwrapped, thickness information $\Delta t(x,y)$ is computed by knowing the refractive index step value ($\Delta n = n_{sample} - n_{medium}$) introduced by the sample (microbead) regarding the surrounding medium (aqueous solution) at the illumination wavelength by means of

$$\Delta\varphi(x,y) = \frac{2\pi}{\lambda}\Delta n \, \Delta t(x,y) \Rightarrow \Delta t(x,y) = \frac{\lambda}{2\pi\,\Delta n}\Delta\varphi(x,y) \textbf{ (1)}$$

Since we are using a silica microbead of $n_{sample} \cong 1.454$ in aqueous-based solution ($n_{medium} \cong 1.33$), the maximum thickness value can be directly computed from Eq. 1 considering that the maximum phase delay is produced at the center of bead. Taking a look at Fig. 2c and leaving aside border bead effects, there are a total number of 7 phase steps in addition with the central phase delay that does not arrive to be a complete phase step. From Eq. 1, the thickness at the bead center equals to 44 and 49 µm considering 7 and 7.8 phase steps, respectively. These values are in good agreement with the theoretical microbead diameter considering that there is a bead manufacturing tolerance and the fact that the refractive index values are approximated. Note that temperature and exact composition of the aqueous-based medium will slightly modify the considered values.
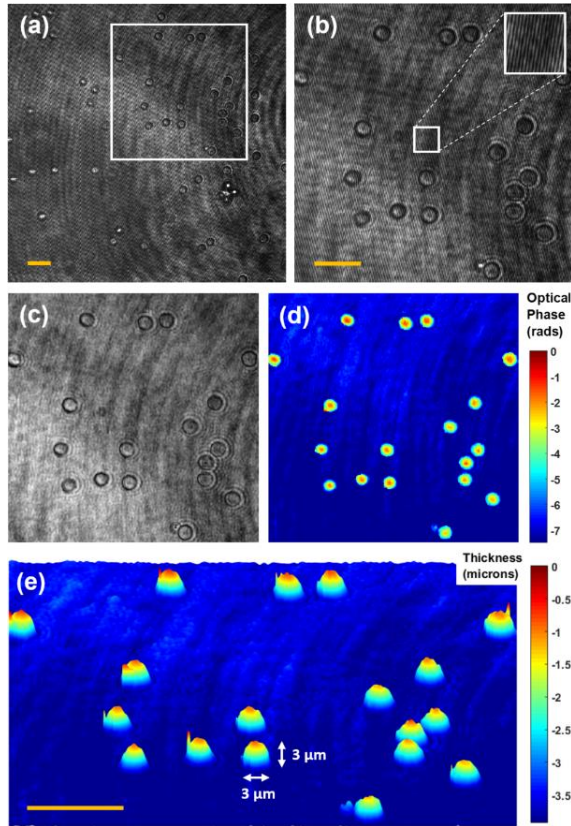

Fig. 3. Experimental results involving 3 µm diameter beads imaged by DHM: (a) the recorded hologram; (b) the ROI marked with a solid line white rectangle in (a) where the inset shows the interferometric fringes; (c) and (d) the retrieved amplitude and unwrapped phase distributions from (b), respectively; and (d) the 3D thickness plot computed from (d). Orange scale bars are 10 µm.

A second calibration experiment involving polystyrene ($n_{sample} = 1.579$) microbeads of 3 µm in diameter is performed. The results are included in Fig. 3 where the recorded hologram is included in (a) and the ROI marked with the solid line white rectangle is magnified in (b) showing also the interferometric fringes. Once FT, filtering, centering and inverse FT is performed (not included at Fig. 3), the retrieved amplitude and unwrapped phase distributions of the ROI included in (b) are presented in (c) and (d), respectively. Finally, thickness distribution is included in (e) showing again concordance at maximum thickness values as it corresponds with 3 µm diameter microbeads. Note that the peaks appearing in some beads are due to phase-unwrapping problems.

In a third calibration experiment, we have used a conical bead fabricated in SU-8 photoresist by two-photon lithography (refractive index n = 1.58). The results are presented through Fig. 4. The conical tip has a dimension of 6 x 12 µm (cone base x height) as it can be seen from Fig. 4(a) corresponding with a SEM image of the bead. Same dimensions are retrieved from the thickness info derived from the proposed DHM platform and included at Fig. 4(b). Note that the bead is flat on the cone base meaning that the retrieved thickness becomes, in this case, as the 3D geometry of the bead.
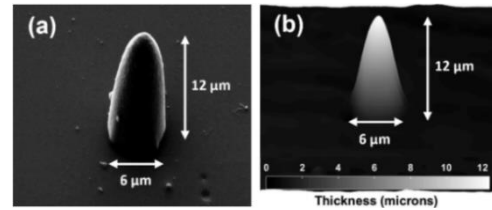

Fig. 4. Experimental results involving a conical bead: (a) SEM image and (b) thickness profile of the bead retrieved from DHM.
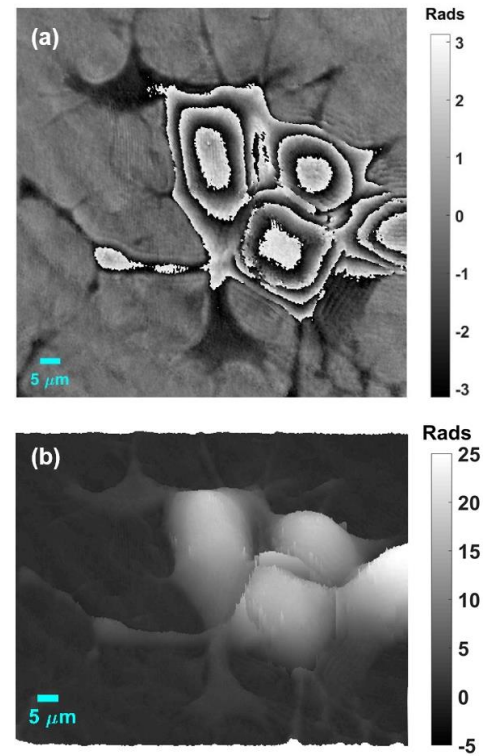

Fig. 5. Experimental results involving a simulated dynamic biosample: (a) 2D wrapped phase (Visualization1.mov) and (b) 3D unwrapped (Visualization2.mov) phase distributions retrieved from DHM.

Finally, an additional experiment concerning a simulated dynamic biosample is included at Fig. 5. The sample consist on hippocampal neuronal cells which are fixed and prepared according to the procedure included in next section, and the sample's movement is induced by a piezo-mirror that shifts the coverslip continuously in time (total recording time: 10 seconds). Figure 5(a) includes the 2D wrapped phase distribution retrieved by the proposed DHM platform while Fig. 5(b) depicts the 3D unwrapped phase profile derived from (a). Those images are the first frames of two video movies named as Vsualization1.mov (4.4MB) and Vsualization2.mov (1.9MB) corresponding with Figs. 5(a) and (b) respectively. One can notice as due to the 3D piezo-induced movement, the sample is not only transversally but also slightly axially shifted, so the sample becomes misfocused as the time is running. But DHM permits to use numerical propagation to refocus the sample. We have implemented numerical refocusing at a given instant (t = 6s) of the video movies. The time line of the videos is stopped, then refocusing is applied, and then the videos restart again. One can see as the thinner terminal branches of the cells are visible after refocusing.

With all these calibration tests, it is experimentally stated that the proposed DHM imaging platform perfectly retrieves the phase values introduced by the studied samples (microbeads and neuron cells). Phase values are converted into thickness results showing good agreement with, on one hand, the theoretical beads dimensions and, on the other hand, with the shape of the conical bead provided by SEM. So, the DHM platform becomes validated from a quantitative point of view.

B. Results using static samples

After validating our home-built DHM layout from a quantitative phase imaging point of view, we have performed additional experiments concerning a wide variety of static biosamples. This subsection includes, as examples, the simultaneous results provided by our single-shot dual-mode water-immersion microscopy platform.

All cell types are, first of all, grown on glass coverslips and kept at 37°C, 5% CO_2 in an incubator for 24-48 hours. Coverslips are then removed from the incubator and inspected under an inverted light microscope to verify the viability and desired appearance of the cells. The cells are then rinsed with Phosphate Buffered Saline (PBS) and subsequently fixed in 4% paraformaldehyde in PBS solution for 15-20 minutes at room temperature. After abundant washing with PBS the coverslips are mounted with VectaShield mounting medium and inverted onto glass slides for imaging.

Figure 6 includes the experimental images for NG108 neuroblastoma cells (upper row), breast cancer cells (central row) and hippocampal neuron cells (lower row) regarding (a)-(d)-(g) bright field imaging modality provided by incoherent illumination and (b)-(e)-(h) and (c)-(f)-(i) the 2D and 3D, respectively, quantitative phase images incoming from the unwrapped phase distribution provided by DHM. Positive and negative visualization modes for 2D quantitative phase imaging and different colormaps for 3D views are selected to enhance image visualization.
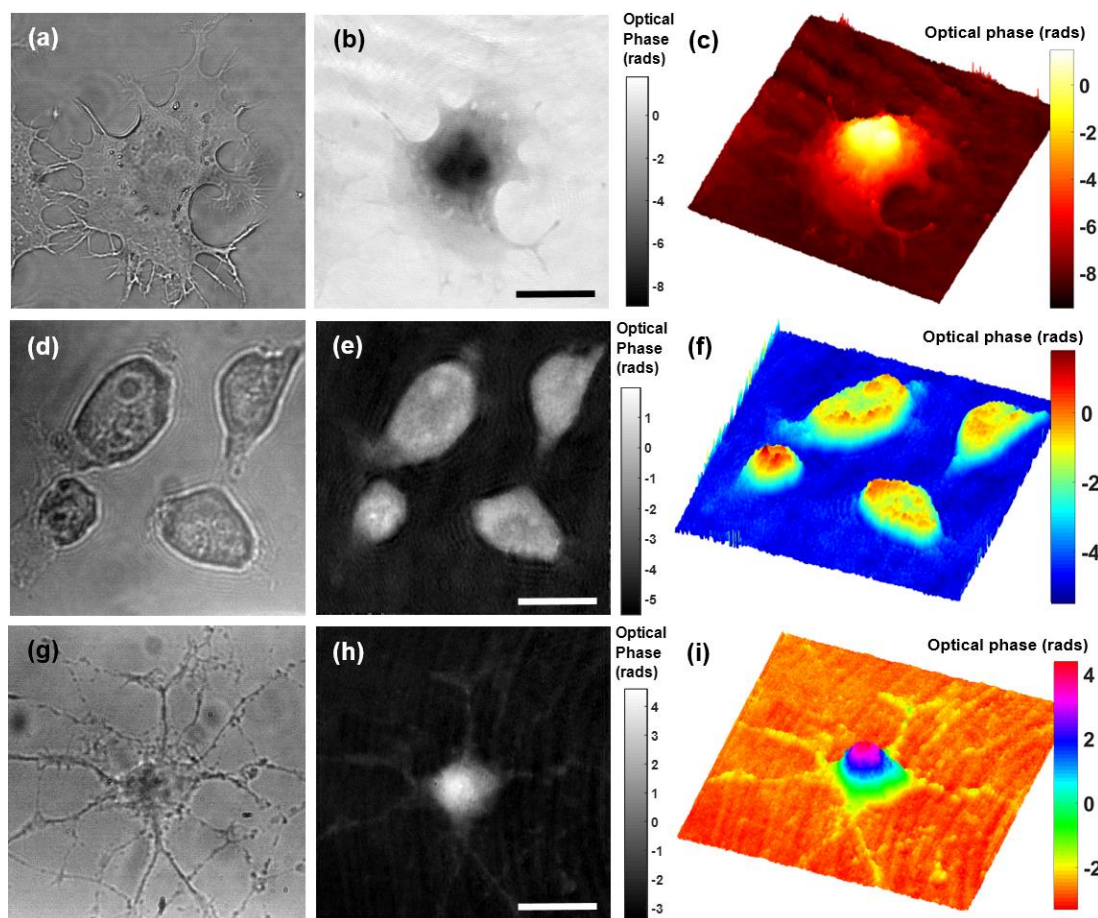

Fig. 6. Experimental results involving biosamples: (a)-(b)-(c), (d)-(e)-(f) and (g)-(h)-(i) are, in the same order, the bright field (intensity) image provided by white light illumination, the 2D quantitative phase imaging provided by DHM and the 3D geometry computed from the phase values for NG108 neuroblastoma cells (first row), breast cancer cells MDA-MB 231 (second row) and hippocampal neuronal cells (third row), respectively. Scale bars (white solid lines) at the lower right corner of (b)-(e)-(h) represent 15 μm.

C. Results with dynamic samples

Finally, to check the capability of the proposed imaging platform regarding single-shot operating principle, Figure 7 includes the experimental results obtained with an additional experiment involving a hippocampal neuron for investigating the cell dynamics. Figures 7(a)-(b) present the first frame of a video movie (Vsualization3.mov, 6.7MB) including the white light imaging and the retrieved phase distribution from DHM concerning the neuron cell movement, respectively. The frame rate of the camera is 12 fps and the total recording time of the movie is 100 seconds. However, video movie is displayed not at real time to reduce its final size. It is difficult to observe the cell movement because of its slowness even with the increased frames per second visualization rate.
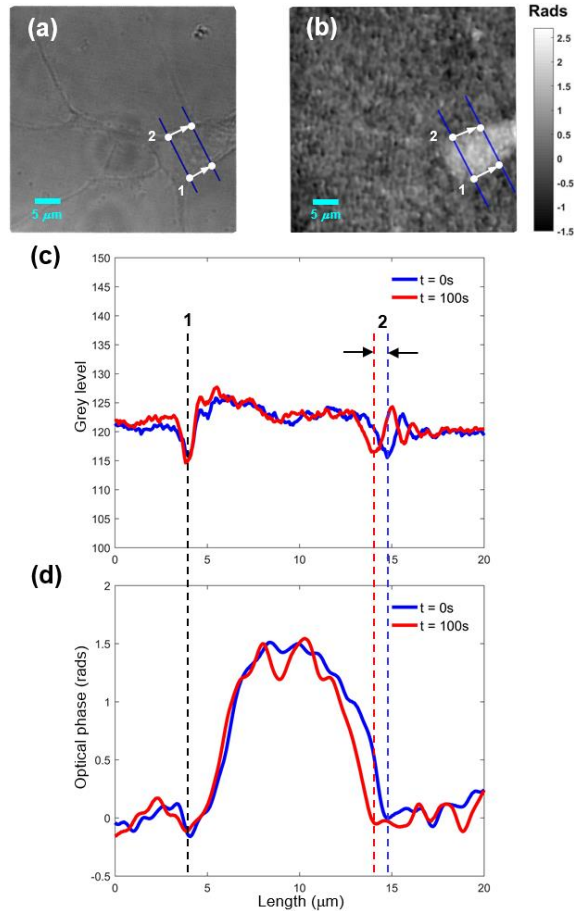

Fig. 7. Experimental results involving a dynamic biosample (hippocampal neuron): (a) intensity image provided by the white light visualization mode, (b) retrieved phase distribution from DHM, and (c)-(d) averaged plots along the points 1 and 2 of the intensity and phase images, respectively, and for the first (t = 0s) and the last (t = 100s) frames of the whole video sequence. Visualization3 includes image sequences presented in (a)-(b).

For this reason, we present at Figs.7(c)-(d) the plots of the first (t = 0s) and last (t = 100s) video frames along the solid blue lines included at Figs. 7(a)-(b), respectively, the first corresponding with the intensity image provided by the white light imaging mode while the second one deriving from the phase distribution retrieved from DHM. Note that we have included the averaged plots included in between the solid blue lines (plot along the white arrows) because plotting a single section is mainly dominated by noise. By paying attention at the averaged points

1 and 2 at the plots, one can see the contraction of the cell's wall after the recording time. Point number 1 is at the same position along the whole movie while point number 2 is slightly shifted from the first frame to the last one. This shift can be seen at both imaging modes (dark shapes with white light and increasing phase values from the background with DHM) and it is quantified in 0.75 μm of cell contraction, approximately, defining an averaged cell's contraction speed of 7.5 nm/s during the total recording time.

4. CONCLUSIONS

We have presented a home-built microscope platform based on the combination of DHM with regular broadband imaging for quantitative and qualitative analysis of biosamples. The proposed imaging platform is capable of working in a single illumination shot thus allowing inspection and analysis of dynamic samples with the only limitation of the acquisition rate of the camera. The resolution limit of the imaging platform is optimized by using a water-immersion objective lens and the interferometric setup is assembled after passing through the imaging lens thus reducing the sensitivity of the DHM layout to vibrations or thermal changes. In order to prove the capabilities of the proposed dual mode microscope platform, we have presented experimental validation of the DHM part considering different types of microbeads (spherical and one cone tip) and fixed cells (neuroblastoma, breast cancer cells and hippocampal neuronal cells) for calibration and biomedical sample testing purposes.

From the reported experiments, it is noticeable that the phase image SNR is lower for the dynamic sample than the fixed one. Fixed samples are placed on a microscope slide and a coverslip is used to enclose the static sample. Thus, both sides of the chamber are optical quality glasses providing low wavefront disturbances. On the contrary, the dynamic sample experiment was implemented using water flow containing physiological nutrients for the living cells. This water flow introduces stronger phase disturbances that reduces SNR in comparison with the static experiments.

Finally, the proposed dual mode microscope platform can present some limitations for certain live cell imaging applications. For instance, long-term time-lapse imaging is highly challenging because of the stabilization complexity of the system conditions. Thus, sterile conditions, sample temperature preservation and liquid evaporation in the immersed microscope objective should be carefully taken into account.

References

1. V. Magidson, and A. Khodjakov, "Circumventing photodamage in live-cell microscopy," Methods Cell. Biol., **114**, 545–60 (2013).
2. S. Wäldchen, J. Lehmann, T. Klein, S. van de Linde, and M. Sauer, "Light-induced cell damage in live-cell super-resolution microscopy," Sci. Rep. **5**, 15348 (2015).
3. M. Mathew, I. Amat-Roldan, R. Andrés, S. I. Santos, D. Artigas, and E. Soriano, "Signalling effect of NIR pulsed lasers on axonal growth," J. Neurosci. Meth. **18**, 196–201 (2010).

4. M. Uyuklu, M. Canpolat, H. J. Meiselman, and O. K. Baskurt, "Wavelength selection in measuring red blood cell aggregation based on light transmittance," J. Biomed. Opt. **16**, 117006 (2011).

5. G. von Bally, "Holography in Medicine and Biology," Berlin, Springer, (1979).

6. M. K. Kim, "Digital Holographic Microscopy: Principles, Techniques, and Applications," 1st ed. New York, Springer (2011).

7. N. T. Shaked, Z. Zalevsky, and L. L. Satterwhite, "Biomedical Optical Phase Microscopy and Nanoscopy," Oxford, Academic Press (2012).

8. C. Mann, L. Yu, C. Lo, and M. Kim, "High-resolution quantitative phase-contrast microscopy by digital holography," Opt. Express **13**, 8693-8 (2005).

9. P. Marquet, B. Rappaz, P. J. Magistretti, E. Cuche, Y. Emery, T. Colomb, and C. Depeursinge, "Digital holographic microscopy: a noninvasive contrast imaging technique allowing quantitative visualization of living cells with subwavelength axial accuracy," Opt. Lett. **30**, 468–70 (2005).

10. P. Ferraro, S. Grilli, D. Alfieri, S. de Nicola, A. Finizio, G. Pierattini, B. Javidi, G. Coppola, and V. Striano, "Extended focused image in microscopy by digital holography," Opt. Express **13**, 6738-49 (2005).

11. F. Charrière, F. Montfort, J. Kühn, T. Colomb, A. Marian, E. Cuche, P. Marquet, and C. Depeursinge, "Cell refractive index tomography by digital holographic microscopy," Opt. Lett. **31**, 178–80 (2006).

12. B. Kemper, and G. von Bally, "Digital holographic microscopy for live cell applications and technical inspection," Appl. Opt. **47**, A52–A61 (2008).

13. M. K. Kim, "Principles and techniques of digital holographic microscopy," SPIE Rev. **1**, 018005 (2010).

14. D. Boss, J. Kühn, P. Jourdain, C. Depeursinge, P. J. Magistretti, and P. Marquet, "Measurement of absolute cell volume, osmotic membrane water permeability, and refractive index of transmembrane water and solute flux by digital holographic microscopy," J. Biomed. Opt. **18**, 036007 (2013).

15. J. W. Goodman, and R. W. Lawrence, "Digital image formation from electronically detected holograms," Appl. Phys. Lett. 11, 77-9 (1967).

16. T. Huang, "Digital holography," Proc. IEEE **59**, 1335-46 (1971).

17. T. Zhang, and I. Yamaguchi, "Three-dimensional microscopy with phase-shifting digital holography," Opt. Lett. **23**, 1221-3 (1998).

18. E. Cuche, P. Marquet, and C. Depeursinge, "Simultaneous amplitude-contrast and quantitative phase-contrast microscopy by numerical reconstruction of Fresnel off-axis holograms," Appl. Opt. **38**, 6994-7001 (1999).

19. F. Dubois, L. Joannes, and J. C. Legros, "Improved three-dimensional imaging with a digital holography microscope with a source of partial spatial coherence," Appl. Opt. **38**, 7085-94 (1999).

20. T. Colomb, F. Dürr, E. Cuche, P. Marquet, H. G. Limberger, R. P. Salathé, and C. Depeursinge, "Polarization microscopy by use of digital holography: application to optical-fiber birefringence measurements," Appl. Opt. **44**, 4461-9 (2005).

21. T. Colomb, J. Kühn, F. Charrière, C. Depeursinge, P. Marquet, and N. Aspert, "Total aberrations compensation in digital holographic microscopy with a reference conjugated hologram," Opt. Express **14**, 4300-6 (2006).

22. J. Sheng, E. Malkiel, and J. Katz, "Digital holographic microscope for measuring three-dimensional particle distributions and motions," Appl. Opt. **45**, 3893-901 (2006).

23. P. Ferraro, S. Grilli, D. Alfieri, S. De Nicola, A. Finizio, G. Pierattini, B. Javidi, G. Coppola, and V. Striano, "Extended focused image in microscopy by digital holography," Opt. Express **13**, 6738-49 (2005).

24. G. Coppola, P. Ferraro, M. Iodice, S. De Nicola, A. Finizio, and S. Grilli, "A digital holographic microscope for complete characterization of microelectromechanical systems," Meas. Sci. Technol. **15**, 529-39 (2004).

25. P. Marquet, B. Rappaz, P. J. Magistretti, E. Cuche, Y. Emery, T. Colomb, and C. Depeursinge, "Digital holographic microscopy: a noninvasive contrast imaging technique allowing quantitative visualization of living cells with subwavelength axial accuracy," Opt. Lett. **30**, 468-70 (2005).

26. B. Rappaz, P. Marquet, E. Cuche, Y. Emery, C. Depeursinge, and P. Magistretti, "Measurement of the integral refractive index and dynamic cell morphometry of living cells with digital holographic microscopy," Opt. Express **13**, 9361-73 (2005).

27. Y. C. Lin, and C. J. Cheng, "Determining the refractive index profile of micro-optical elements using transflective digital holographic microscopy," J. Opt. **12**, 115402 (2010).

28. S. Wang, L. Xue, J. Lai, and Z. Li, "Three-dimensional refractive index reconstruction of red blood cells with one-dimensional moving based on local plane wave approximation," J. Opt. **14**, 065301 (2012).

29. H. Iwai, C. Fang-Yen, G. Popescu, A. Wax, K. Badizadegan, R. R. Dasari, and M. S. Feld, "Quantitative phase imaging using actively stabilized phase-shifting low-coherence interferometry," Opt. Lett. **29**, 2399-401 (2004).

30. R. Guo, B. Yao, J. Min, M. Zhou, X. Yu, M. Lei, S. Yan, Y. Yang, and D. Dan, "LED-based digital holographic microscopy with slightly off-axis interferometry," J. Opt. **16**, 125408 (2014).

31. V. Srivastava, T. Anna, and D. S. Mehta, "Full-field Hilbert phase microscopy using nearly common-path low coherence off-axis interferometry for quantitative imaging of biological cells," J. Opt. **14**, 125707 (2012).

32. S. Reichelt, and H. Zappe, "Combined Twyman-Green and Mach-Zehnder interferometer for microlens testing," Appl. Opt. **44**, 5786-92 (2005).

33. G. Popescu, T. Ikeda, R. R. Dasari, and M. S. Feld, "Diffraction phase microscopy for quantifying cell structure and dynamics," Opt. Lett. **31**, 775-7 (2006).

34. V. Mico, Z. Zalevsky, and J. Garcia, "Common-path phase-shifting digital holographic microscopy: A way to quantitative phase imaging and superresolution," Opt. Commun. **281**, 4273-81 (2008).

35. V. Mico, Z. Zalevsky, P. García-Martínez, and J. García, "Synthetic aperture superresolution with multiple off-axis holograms," J. Opt. Soc. Am. A **23**, 3162-70 (2006).

36. V. Mico, Z. Zalevsky, and J. García, "Synthetic aperture microscopy using off-axis illumination and polarization coding," Opt. Commun. **276**, 209-17 (2007).

37. P. Gao, I. Harder, V. Nercissian, K. Mantel, and B. Yao, "Phase-shifting point-diffraction interferometry with common-path and in-line configuration for microscopy," Opt. Lett. **35**, 712-4 (2010).

38. N. T. Shaked, "Quantitative phase microscopy of biological samples using a portable interferometer," Opt. Lett. **37**, 2016-8 (2012).

39. B. Bhaduri, C. Edwards, H. Pham, R. Zhou, T. H. Nguyen, L. L. Goddard, and G. Popescu, "Diffraction phase microscopy: principles and applications in materials and life sciences," Adv. Opt. Photon. **6**, 57-119 (2014).

40. S. Bernet, A. Jesacher, S. Fürhapter, C. Maurer, and M. Ritsch-Marte, "Quantitative imaging of complex samples by spiral phase contrast microscopy," Opt. Express **14**, 3792-805 (2006).

41. G. Popescu, L. P. Deflores, J. C. Vaughan, K. Badizadegan, H. Iwai, R. R. Dasari, and M. S. Feld, "Fourier phase microscopy for investigation of biological structures and dynamics," Opt. Lett. **29**, 2503-5 (2004).

42. H. Ding, and G. Popescu, "Instantaneous spatial light interference microscopy," Opt. Express 18, 1569-75 (2010).

43. D. Fu, S. Oh, W. Choi, T. Yamauchi, A. Dorn, Z. Yaqoob, R. R. Dasari, and M. S. Feld, "Quantitative DIC microscopy using an off-axis self-interference approach," Opt. Lett. **35**, 2370-2 (2010).

44. F. Merola, L. Miccio, M. Paturzo, A. Finizio, S. Grilli, and P. Ferraro, "Driving and analysis of micro-objects by digital holographic microscope in microfluidics," Opt. Lett. **36**, 3079-81 (2011).

45. B. Kemper, A. Vollmer, C. E. Rommel, J. Schnekenburger, and G. von Bally, "Simplified approach for quantitative digital holographic phase contrast imaging of living cells," J. Biomed. Opt. **16**, 026014 (2011).

46. V. Chhaniwal, A. S. G. Singh, R. A. Leitgeb, B. Javidi, and A. Anand, "Quantitative phase-contrast imaging with compact digital holographic microscope employing Lloyd's mirror," Opt. Lett. **37**, 5127-9 (2012).

47. A. S. G. Singh, A. Anand, R. A. Leitgeb, and B. Javidi, "Lateral shearing digital holographic imaging of small biological specimens," Opt. Express **20**, 23617-22 (2012).

48. V. Mico, J. Garcia, and Z. Zalevsky, "Quantitative phase imaging by common-path interferometric microscopy: application to super-resolved imaging and nanophotonics," J. Nanophoton **3**, 031780 (2009).

49. V. Mico, C. Ferreira, Z. Zalevsky, and J. García, "Spatially-multiplexed interferometric microscopy (SMIM): converting a standard microscope into a holographic one," Opt. Express **22**, 14929-43 (2014).

50. J. A. Picazo-Bueno, Z. Zalevsky, J. García, C. Ferreira, and V. Micó, "Spatially-multiplexed interferometric microscopy with partially coherent illumination," J. Bio. Opt. **21**, 106007 (2016).

51. N. T. Shaked, Y. Zhu, N. Badie, N. Bursac, and A. Wax, "Reflective interferometric chamber for quantitative phase imaging of biological sample dynamics," J. Biomed. Opt. **15**, 030503 (2010).

52. U. Schnars, "Direct phase determination in hologram interferometry with use of digitally recorded holograms," J. Opt. Soc. Am. A **11**, 2011–5 (1994).

53. T. Kreis, Handbook of holographic interferometry: optical and digital methods (Wiley-VCH, 2005).

54. V. Micó, Z. Zalevsky, C. Ferreira, and J. García, "Superresolution digital holographic microscopy for three-dimensional samples," Opt. Express **16**, 19260-70 (2008).